


# Simulation study on the impact of microwave pulses on performance of ensemble nitrogen-vacancy centers

Xu-Bo Liao(廖旭博), Yi Zhang(张燚), Qi-Yuan Jiang(江奇渊), Bing-Feng Sun(孙兵锋), Sheng-Bing Shi(史圣兵), Shi-Yu Guan(管世钰), Yu-Xiao Wang(王雨潇), Zhong-Qi Tan(谭中奇), and Jie Yuan(袁杰)

**Citation:**Chin. Phys. B, 2026, 35 (**8**): 080701. DOI: 10.1088/1674-1056/ae24e9
http://cpb.iphy.ac.cn; http://iopscience.iop.org/cpb

**What follows is a list of articles you may be interested in**

---

## Vector-total field magnetometry and calibration using NV center ensembles

Kai-Hui Wang(王凯辉), Yun-Bin Zhu(朱云彬), Zi-Yun Yu(于子云), Xiang Li(李想), Xiang-Mei Xu(许祥妹), Zhao Zhao(赵昭), Liang Zhang(张亮), Ke Jing(靖克), and Yi-Jin Xie(谢一进)

Chin. Phys. B, 2026, 35 (**7**): 070706. DOI: 10.1088/1674-1056/ae12d5

## *In-situ* measurement of cell temperature by spin-relaxation rate analysis for an atomic magnetometer

Bing-Quan Zhao(赵丙权), Zhe Qi(祁喆), Jian-Long Wang(王建龙), Li-Hua Wu(武丽花), Qian-Yun Zhao(赵倩云), Jun-Xin Wei(韦俊新), Wei-Ren Liu(刘为任), and Ling-Xin Kong(孔令鑫)

Chin. Phys. B, 2026, 35 (**6**): 060703. DOI: 10.1088/1674-1056/ae07bf

## Structural optimization of magnetic flux concentrator based on particle swarm optimization algorithm

Yu-Xiao Wang(王雨潇), Shi-Yu Guan(管世钰), Yi Zhang(张燚), Qi-Yuan Jiang(江奇渊), Bing-Feng Sun(孙兵锋), and Zhong-Qi Tan(谭中奇)

Chin. Phys. B, 2026, 35 (**4**): 040701. DOI: 10.1088/1674-1056/ae0b38

## Spin-based magnetic detection of optically trapped single cell in microfluidic channel

Jun Yin(殷俊), Sanyou Chen(陈三友), Yihao Yan(燕一皓), Mengqi Wang(王孟祺), Ya Wang(王亚), Yiheng Lin(林毅恒), Qi Zhang(张琪), and Fazhan Shi(石发展)

Chin. Phys. B, 2025, 34 (**7**): 070704. DOI: 10.1088/1674-1056/adde38

## Visibility enhancement in two-dimensional lensless ghost imaging with true thermal light

Xi-Hao Chen(陈希浩), Ling Yan(燕玲), Wei Wu(吴炜), Shao-Ying Meng(孟少英), Ling-An Wu(吴令安), Zhi-Bin Sun(孙志斌), Chao Wang(王超), Guang-Jie Zhai(翟光杰)

Chin. Phys. B, 2017, 26 (**6**): 060702. DOI: 10.1088/1674-1056/26/6/060702

---

# Simulation study on the impact of microwave pulses on performance of ensemble nitrogen-vacancy centers

Xu-Bo Liao(廖旭博)[1,2,3], Yi Zhang(张燚)[1,2,†], Qi-Yuan Jiang(江奇渊)[1,2], Bing-Feng Sun(孙兵锋)[1,2], Sheng-Bing Shi(史圣兵)[3], Shi-Yu Guan(管世钰)[1,2], Yu-Xiao Wang(王雨潇)[1,2], Zhong-Qi Tan(谭中奇)[1,2], and Jie Yuan(袁杰)[1,2,‡]

[1] *College of Advanced Interdisciplinary Studies, National University of Defense Technology, Changsha* 410073, *China*
[2] *Nanhu Laser Laboratory, National University of Defense Technology, Changsha* 410073, *China*
[3] *The No.* 32201st *Troop of PLA, Baicheng* 137000, *China*

(Received 24 August 2025; revised manuscript received 17 November 2025; accepted manuscript online 27 November 2025)

This study is conducted to establish a reliable simulation model for investigating the impact of microwave pulses on the performance of an ensemble nitrogen-vacancy (NV) center system, thereby providing a basis for optimizing microwave parameters and enhancing quantum sensing performance. The simulation of ensemble NV centers is realized through the design of "Single NV Center Module" + "Ensemble Control Module". Verified by optically detected magnetic resonance (ODMR), Ramsey, and Hahn echo experiments, the program can accurately reproduce the core characteristics of the experiments, confirming the reliability of the model. Using this model to study the influence of microwave spatial inhomogeneity on system performance, it was found that when $\theta$ (the range of microwave axial distribution) is 90°, the sensitivity of the Hahn echo decreases by 3.6 times, and when the amplitude gradient is 50 μT/mm, the sensitivity decreases by 1.8 times, providing quantitative support for optimizing microwave parameters.

**Keywords:** microwave pulse sequences, ensemble NV centers, coherence time, spatial inhomogeneity

**PACS:** 07.55.Ge, 75.40.Mg, 85.75.Ss, 42.50.–p

**DOI:** 10.1088/1674-1056/ae24e9 **CSTR:** 32038.14.CPB.ae24e9

## 1. Introduction

Negatively charged nitrogen-vacancy centers have been extensively studied and applied in fields such as quantum computing, quantum information, magnetic field measurement, and nano-imaging, owing to their significant advantages including room-temperature stability, long quantum coherence time, optical addressability, and biocompatibility.[1–3] The measurement sensitivity of the NV center system is closely related to its coherence, and noise can cause a significant decay of system coherence, thereby reducing measurement performance.[3]

The energy level structure of $NV^-$ centers in diamond is shown in Fig. 1. In addition to the three Zeeman levels of the ground state $^3A^2$ and the excited state $^3E$, it also contains two metastable states, $^1A_1$ and $^1E$. This allows electrons in the excited state to return to the ground state through non-radiative intersystem crossing (ISC) processes, in addition to spontaneous radiative transitions.[3–5] Since the probability of intersystem crossing in the $|m_s = \pm 1\rangle$ excited state is higher than that in the $|m_s = 0\rangle$ state, the population of different spin states can be distinguished by the intensity of spontaneously emitted fluorescence. An applied magnetic field will lift the degeneracy of the $|m_s = \pm 1\rangle$ energy levels. Through 532-nm laser pumping, spontaneous emission, and the ISC process, electrons accumulate in the ground state $|m_s = 0\rangle$ energy level. The pumping rate $\Gamma_p$ is used to represent the rate of transition from the ground states $|m_s = \pm 1\rangle$ to $|m_s = 0\rangle$. Neglecting the influence of the excited state $^3E$ and the metastable states $^1A_1$ and $^1E$, the system can be simplified and described using a three-level model.

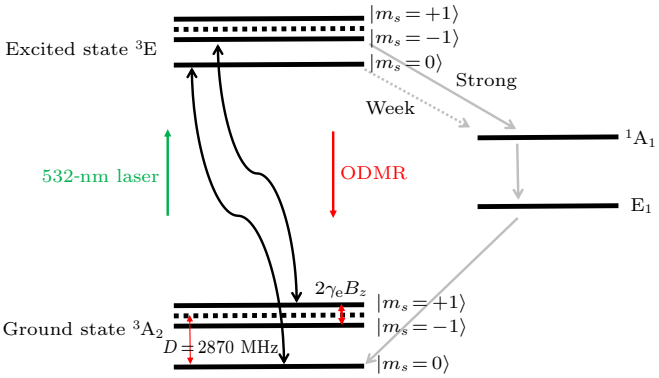



**Fig. 1.** Energy level structure of $NV^-$ centers in diamond.

In the study of diamond NV centers, the coherence decay characteristics of spin systems are typically characterized by $T_2^*$ and $T_2$.[6] $T_2^*$ is the spin free induction decay time (also known as dephasing time), which describes the decay of

†Corresponding author. E-mail: abnormal_zy@163.com
‡Corresponding author. E-mail: jieyuan@nudt.edu.cn

© 2026 Chinese Physical Society and IOP Publishing Ltd. All rights, including for text and data mining, AI training, and similar technologies, are reserved.

phase coherence in a spin system under the combined action of static inhomogeneous magnetic fields and dynamic noise. Its rapid decay stems from external static magnetic field inhomogeneities (such as magnetic field gradients) and internal dynamic noise (such as spin bath fluctuations). $T_2$ is the spin-spin relaxation time (also known as decoherence time). The difference from $T_2^*$ is that the influence of static magnetic field inhomogeneity can be eliminated through pulse sequences such as spin echo, which only reflects the decay of spin coherence under the action of dynamic noise. Generally, $T_2^* \ll T_2$, near-surface NV centers have $T_2^*$ values of only 3 μs∼ 50 μs.[3] After spin-echo processing, $T_2$ can be improved to 100 μs∼ 200 μs,[7,8] while dynamic decoupling sequences (*e.g.*, CPMG, XY8) can further suppress noise from spin baths and other dynamic sources, extending $T_2$ to the millisecond level. $T_2$ is a core metric for evaluating quantum sensor performance, directly determining the detection sensitivity.[1] For the ensemble NV centers system, the sensitivities of measuring the magnetic field by the continuous-wave ODMR (CW-ODMR), Ramsey, and Hahn echo methods are[9–11]

$$\begin{cases} \eta_{\mathrm{CW-ODMR}}^{\mathrm{ensemble}} \approx \dfrac{4}{3\sqrt{3}} \dfrac{\Delta\upsilon}{C\sqrt{R}} \dfrac{\hbar}{g_e\mu_B}, \\ \eta_{\mathrm{Ramsey}}^{\mathrm{ensemble}} \approx \dfrac{\hbar}{g_e\mu_B} \dfrac{1}{\Delta m_s} \dfrac{1}{C\sqrt{N}} \dfrac{1}{\mathrm{e}^{-(\tau/T_2^*)^\alpha}} \dfrac{\sqrt{t_I+\tau+t_R}}{\tau}, \\ \eta_{\mathrm{Hahn}}^{\mathrm{ensemble}} \approx \dfrac{\pi}{2} \dfrac{\hbar}{g_e\mu_B} \dfrac{1}{C\sqrt{N}} \dfrac{1}{\mathrm{e}^{-(\tau/T_2)^\alpha}} \dfrac{\sqrt{t_I+\tau+t_R}}{\tau}, \end{cases} \tag{1}$$

where $\hbar/g_e\mu_B$ is the basic constant term, $g_e \approx 2.003$ is the electronic $g$ factor of the nitrogen-vacancy center, $\mu_B$ is the Bohr magneton, and $\hbar$ is the reduced Planck constant, $R$ is the photon detection rate, $\Delta\upsilon$ is the linewidth of the ODMR spectrum, $C$ is the signal contrast, $\alpha$ is the decay stretching exponent, and $\tau$ is the free precession time of each measurement, $t_I$ is the initialization time, and $t_R$ is the readout time. To extend to spins with higher multiplicities, the spin state difference $\Delta m_s \geq 2$ for interferometric measurement is used. For negligible $t_I$ and $t_R$, the optimal measurement times are $\tau = T_2^*/2$ and $\tau = T_2$, respectively. $N$ is the number of NV centers.[12] Equation (1) can be simplified as

$$\begin{cases} \eta_{\mathrm{CW-ODMR}}^{\mathrm{ensemble}} \propto \dfrac{\Delta\upsilon}{C}, \\ \eta_{\mathrm{Ramsey}}^{\mathrm{ensemble}} \propto \dfrac{\mathrm{e}^{(1/2)^\alpha}}{C\cdot\sqrt{T_2^*}}, \\ \eta_{\mathrm{Hahn}}^{\mathrm{ensemble}} \propto \dfrac{1}{C\cdot\sqrt{T_2}}. \end{cases} \tag{2}$$

Based on the derivation using the density matrix and Schrödinger equation (see Appendix A), we obtain the time evolution relationship of the Ramsey signal in an ensemble NV centers system[10,13,14]

$$S_{\mathrm{Ramsey}}(\tau) = \frac{S_0}{2}\left[1 - C\cdot \mathrm{e}^{-(\tau/T_2^*)^\alpha}\cos(\omega_x\tau)\right]. \tag{3}$$

The relationship between Hahn echo signal and time variation is given by[15]

$$S_{\mathrm{Hahn}}(\tau) = S_0\cdot \mathrm{e}^{-(\tau/T_2)^\alpha}, \tag{4}$$

where $S_0$ is the background fluorescence signal baseline, $C$ is the contrast, $\omega_x$ is the Rabi oscillation angular frequency, and $\alpha$ is a numerical factor related to the specific noise type. The stretched exponent $\alpha$ for Hahn echo decay varies between 0.5 and 3.[10,16]

## 2. Methods

The density matrix evolution kinetic equation of the three-level model $\dot{\rho} = f(\rho)$ is derived from the eigen-Hamiltonian. For the detailed derivation process, please refer to Appendix A. For the ensemble NV centers system, it is necessary to establish an output fluorescence intensity function. The fluorescence intensity is affected by multiple factors such as microwave power, microwave frequency, and magnetic field. The ensemble fluorescence intensity is composed of the superposition of the output fluorescence intensities of each single NV center in the system. Therefore, for the NV centers with different parameter gradients, the ensemble fluorescence intensity can be calculated by means of weighted average. The final expression of the system's output fluorescence intensity is

$$I_{\mathrm{En}} = \sum k_i I_i, \tag{5}$$

where $k_i$ is the light intensity weighting coefficient occupied by the NV center, and $\sum k_i = 1$, $I_i$ are the fluorescence intensities.

We modularly design the ensemble NV center simulation model. The orange block on the right side of Fig. 2 in the structural block diagram is the single NV center simulation module. The physical effect module simulates physical effects such as pump light, external magnetic field, and microwave pulses respectively. The physical effect module regulates the system evolution by modifying Hamiltonian parameters. The main parameters include system parameters (longitudinal relaxation rate $\gamma_1$, transverse relaxation rate $\gamma_2$, and pump rate $\gamma_p$), magnetic field parameters (NV axial magnetic field $B_z$, magnetic field noise $\Delta B_z$), and microwave parameters (microwave magnetic field $B_x$, $\pi$ pulse width $t_\pi$, pulse axial deviation $\theta$, and microwave frequency $\omega_x$). The noise source module is used to generate magnetic field noise $\Delta B_z$. We mainly considered the presence of spin bath fluctuations around the NV center, which is the main cause of dephasing. In this paper, the Ornstein–Uhlenbeck (OU for short) process is used to generate random magnetic field noise $\Delta B_z(t)$, with parameters including coupling strength $b$, correlation time $\tau_c$.[15,17] The RK4 algorithm module is employed to solve the time evolution equation of

the density matrix, thus ensuring the accuracy of numerical calculations. The signal acquisition module simulates the experimental measurement process and computes the observable quantities of the system. The fluorescence intensity reading module calculates the fluorescence signal based on the density matrix, thus realizing the connection between the theoretical model and experimental observation.

The green block on the left side of Fig. 2 is the ensemble NV centers simulation module, which realizes the simulation of ensemble output characteristics by integrating multiple single NV center models. Among them, the ensemble control module provides differentiated parameter inputs for different single NV center modules by reasonably setting parameters such as light intensity weight, static magnetic field noise, microwave amplitude noise, and microwave frequency noise. The parameter distribution module generates the parameter distribution of each NV center in the ensemble. The parallel computing engine efficiently completes the parallel computing of a large number of NV centers. The ensemble result synthesis module integrates the calculation results of individual NV centers according to weights to obtain the ensemble average signal. This modular design endows the system with good scalability and maintainability, facilitating the subsequent integration of new physical effects or optimization of algorithms.

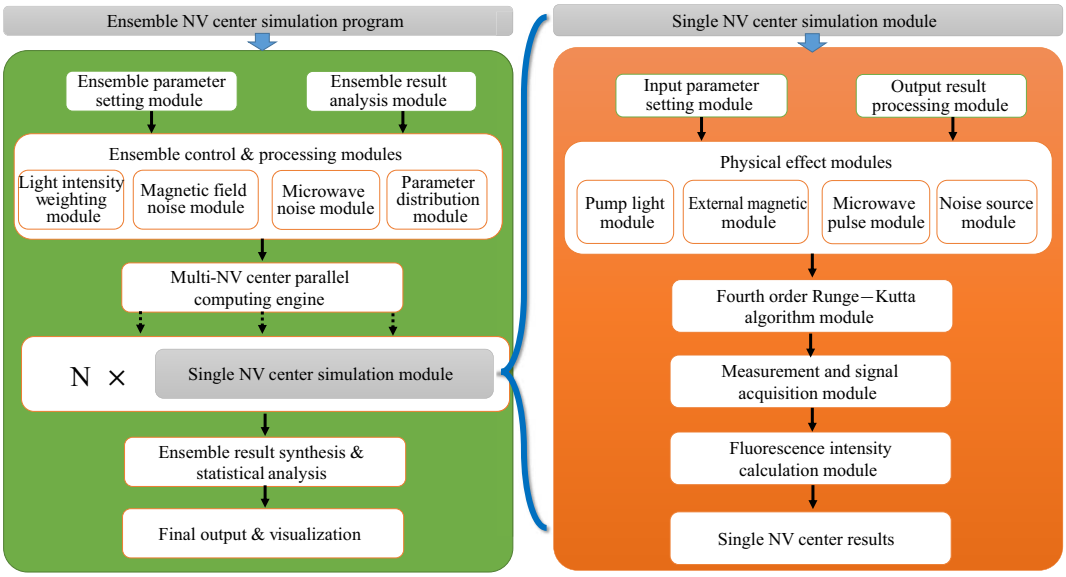



**Fig. 2.** Structure block diagram of the ensemble NV centers simulation model. The green block on the left consists of the ensemble NV centers simulation module, and the red block on the right consists of the single NV center simulation module.

We have built a cage-based optical system for diamond NV center experiments. By comparing the simulation results with the experimental output, we verify the reliability of the simulation model. The structure is shown in Fig. 3. The system consists of an optical module, a microwave module, a control and acquisition module, and a power supply module. The optical module includes a laser pulse generator, a cage-based optical setup, a microwave radiation structure, a diamond sample, and a photodetector. The microwave radiation structure adopts double split-ring resonators from CIQTEK.[18,19] The diamond sample DNV$^{\mathrm{TM}}B1$ is produced by Element Six, with dimensions of 5 mm×5 mm×0.5 mm. The laser is a 532-nm solid-state laser, and the maximum laser power is 100 mW. The laser pulse generator emits green laser light, which excites the NV centers to generate red fluorescence. After the fluorescence is filtered by a filter, it is focused by a lens onto a photodetector, which completes the conversion of optical signals to electrical signals and the reading of fluorescence intensity.

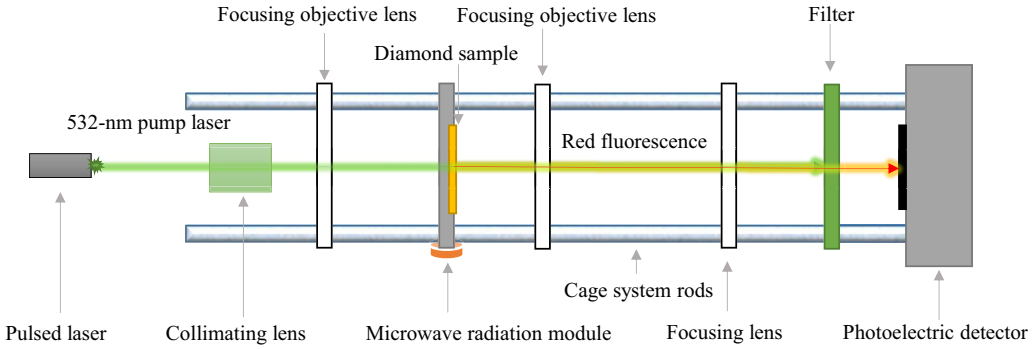



**Fig. 3.** Structural diagram of the experimental system.

## 3. Application and analysis

### 3.1. Verification of the reliability of the simulation program

Under zero-field conditions, the system's ODMR spectra were tested at microwave powers of 26 dBm, 23 dBm, 20 dBm, and 17 dBm, respectively (the microwave power here refers to the microwave power applied to the NV center sample after passing through the power amplifier, not the power value set at the microwave source). Through Rabi oscillation experiments, the corresponding Rabi frequencies $\Omega_{\text{Rabi}}$ were measured as 2.81 MHz, 1.99 MHz, 1.41 MHz, and 1.06 MHz, and the full width at half maximum (FWHM) $\Delta\upsilon$ of the spectrum under each state was obtained. When simulating the ODMR experiment, in order to approximate the characteristics of the real experimental system, the core parameters are set as $\gamma_1 = 1000\ \text{s}^{-1}$, $\gamma_2 = 25000\ \text{s}^{-1}$, $\gamma_\text{p} = 50000\ \text{s}^{-1}$. Specific parameter settings for the experiment and simulation are compared in Table 1. Based on the Rabi frequency obtained from the experiment, the corresponding microwave magnetic fields obtained through simulation inversion were 100 μT, 71 μT, and 38 μT, respectively. Then, the simulated ODMR spectra are plotted, and the result data are normalized. The comparison of the output curves of the experimental system and the simulation program is shown in Fig. 4.

**Table 1.** Parameter settings of experimental system and simulation program.

| Experimental | | | Simulation | | |
|---|---|---|---|---|---|
| $P_{\text{MW}}$ (dBm) | $\Omega_{\text{Rabi}}$ (MHz) | $\Delta\upsilon$ (MHz) | $B_x$ (μT) | $\Omega_{\text{Rabi}}$ (MHz) | $\Delta\upsilon$ (MHz) |
| 26 | 2.81 | 12.8 | 100 | 2.81 | 13 |
| 23 | 1.99 | 12 | 71 | 1.99 | 12 |
| 20 | 1.41 | 11.6 | 50 | 1.41 | 11.5 |
| 17 | 1.06 | 11.6 | 38 | 1.06 | 11.5 |

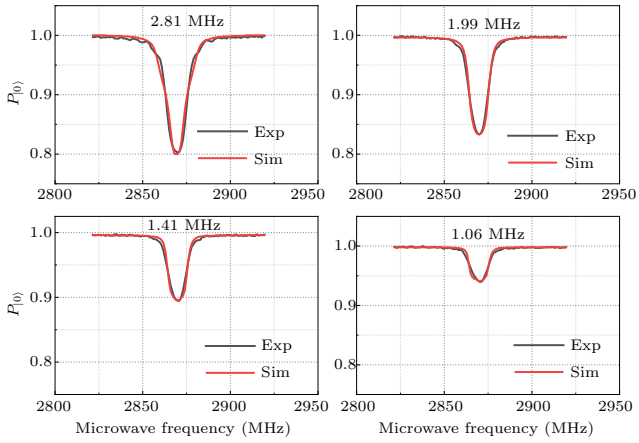



**Fig. 4.** Comparisons of experimental and simulated ODMR spectra. The abscissa is the microwave frequency, and the ordinate is the population probability of the $|0\rangle$ state. The black solid line represents the experimental results, and the red solid line represents the simulation results.

Adjust the microwave power so that the Rabi frequency is $\Omega_{\text{Rabi}} = 9.25$ MHz, and set the microwave frequency to $\omega_x = 2.87$ GHz. In the simulation program, set the corresponding microwave magnetic field strength to $B_x = 330$ μT, and keep the rest of the parameters consistent with those in the ODMR experiment. Figure 5(a) shows the comparison of the Ramsey experiment results between the experimental system and the simulation program (the abscissa is the free evolution time, and the ordinate is the normalized fluorescence intensity). The red scatter curve is the output result of the experimental system, and the black solid line is the output result of the simulation program. The fitted dephasing times are $T^*_{2\text{real}} = 50.7$ ns and $T^*_{2\text{sim}} = 48.8$ ns.

The Hahn echo experiment adopts the same parameter settings as the Ramsey experiment. Figure 5(b) shows the comparison of the Hahn echo experiment results between the experimental system and the simulation program (the abscissa is the free evolution time, and the ordinate is the normalized fluorescence intensity). The black scatter curve is the output result of the experimental system, and the red solid line is the output result of the simulation program. The fitted decoherence times $T_{2\text{real}} = 39.2$ μs, $T_{2\text{sim}} = 39.9$ μs. Based on the comparative results of the ODMR experiment, Ramsey experiment, and Hahn echo experiment, the simulation program designed in this paper can accurately reproduce the core characteristics of the experimental system.

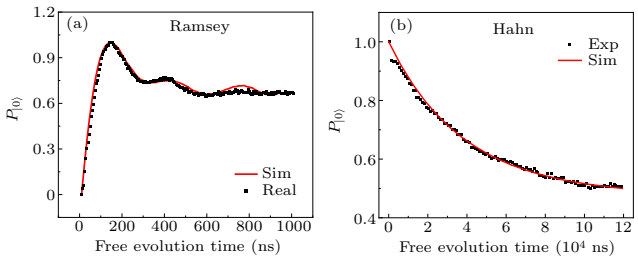



**Fig. 5.** Comparisons of experimental and simulation outputs. The black dashed line represents the experimental results, and the red solid line represents the simulation results. (a) Comparison of Ramsey curves, (b) comparison of Hahn echo curves.

### 3.2. Ensemble multi-peak ODMR and hyperfine coupling simulation

In the diamond NV center sample, there are four NV axes $\alpha$, $\beta$, $\gamma$, $\delta$, and the angle between each pair of these four axes in space is 109°.[20] The relative positional relationship between different axes in the ensemble within a magnetic field is shown in Fig. 6(a). To simplify the research, we assume that the static magnetic field $B_z$ is parallel to the $\alpha$-axis, and the microwave field $B_{\text{MW}}$ is perpendicular to the $\alpha$-axis.

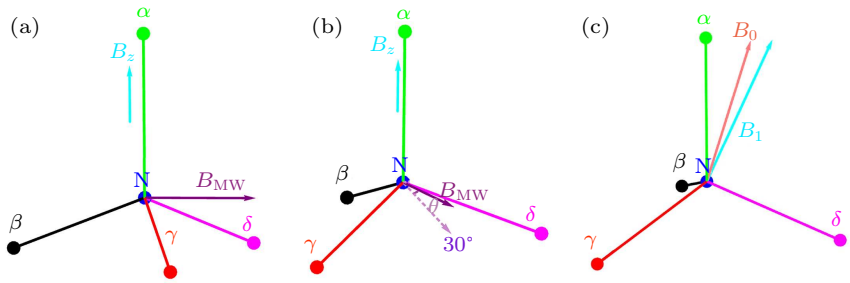



**Fig. 6.** (a) In the diamond ensemble NV centers, the $\alpha$-axis is parallel to the static magnetic field $B_z$ and perpendicular to the microwave magnetic field $B_{MW}$; (b) Schematic diagram of the inhomogeneous axial spatial distribution of the microwave magnetic field, where the dashed line represents $B_{MW}$ when the maximum deviation angle is 30°; (c) The static magnetic field $B_0$ forms unequal angles with the four axes, and shifts by a small angle to $B_1$.

Owing to the hyperfine coupling between the electron spin of the NV center and the $^{14}$N nuclear spins ($I = 1$), the resonance peak after the Zeeman splitting of the NV center is further split into three hyperfine peaks with a peak interval of 2.2 MHz.[15,21] Figure 7(a) shows the ensemble ODMR spectrum when $B_z = 11.4$ mT, $B_{MW} = 50$ μT. Since the static magnetic field has equal angles with the axes $\beta$, $\gamma$, $\delta$, its projections onto these axes are equal, so the resonance peaks completely overlap, ultimately presenting 2 pairs of resonance peaks, which are the resonance peak of the NV-$\alpha$ and the superimposed resonance peaks of the NV-$\beta$, $\gamma$, $\delta$. Zooming the $\alpha$-axis resonance peak at a microwave frequency of 2550 MHz reveals three hyperfine peaks with unequal intensities, and their resonance frequencies correspond to 2548.3 MHz, 2550.5 MHz, and 2552.7 MHz, respectively. Its mechanism is that when the static magnetic field meets the polarization transfer threshold, the laser polarizes the NV electron spins, and the electron spins indirectly polarize the $^{14}$N nuclear spins through hyperfine coupling, resulting in population bias. Here, we refer to De Lange G 2010 Science 330 60–3, where the population ratio of $^{14}$N nuclear spins on each energy level ($m_I = |+1\rangle, |0\rangle, |-1\rangle$) is 5:3:2.[15,20] In the simulation, we achieve this by setting magnetic field offsets and light intensity weighting coefficients.

In contrast, in Fig. 7(b), when $B_z = 2$ mT, $B_{MW} = 50$ μT, the population of nuclear spins in each energy level tends to be equal, showing three hyperfine peaks with equal intensities. Figure 6(b) shows that the microwave field has axial inhomogeneity in space, and its influence on the output characteristics of the ensemble is discussed in Subsection 3.2 of this paper. Figure 6(c) shows that when the static magnetic field has unequal angles with the four NV axes, the ODMR spectrum in Fig. 7(c) presents 4 pairs of resonance peaks. When the static magnetic field $B_0$ deviates by a small angle from the magnetic field $B_1$, each angle changes, the projection of the static magnetic field on each axis changes, and the positions of the corresponding 4 pairs of peaks also change accordingly.

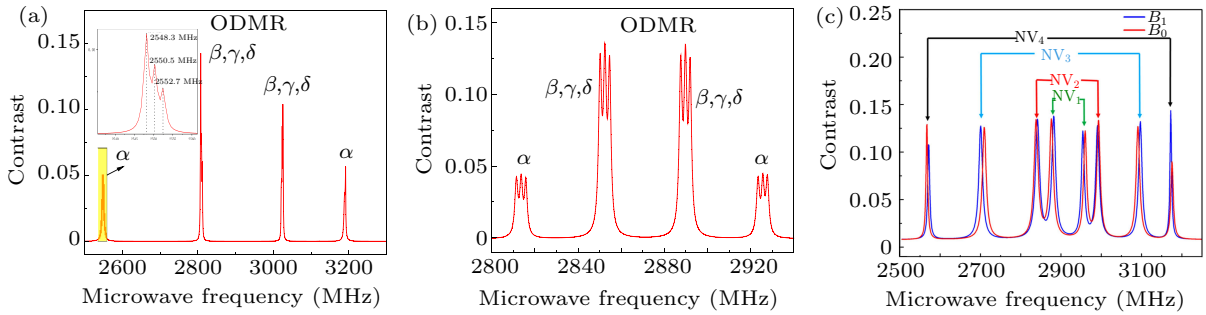



**Fig. 7.** Ensemble ODMR spectrum, with the abscissa being microwave frequency and the ordinate being contrast. (a) The static magnetic field $B_z = 11.4$ mT and microwave field $B_{MW} = 50$ μT; (b) $B_z = 2.0$ mT and $B_{MW} = 50$ μT; (c) $B_0 = B_1 = 11.4$ mT and $B_{MW} = 330$ μT.

### 3.3. Inhomogeneous spatial distribution of microwaves

In this article, we do not consider the spatial inhomogeneity of the static magnetic field, only discuss the impact of the spatial inhomogeneity of the microwave magnetic field on the system. The system parameters are as follows: longitudinal relaxation rate $\gamma_1 = 1000$ s$^{-1}$, transverse relaxation rate $\gamma_2 = 2.5 \times 10^5$ s$^{-1}$, and pumping rate $\gamma_p = 5 \times 10^5$ s$^{-1}$. The magnetic field parameters: microwave magnetic field $B_x = 330$ μT and static magnetic field $B_z = 2$ mT. Noise module parameters: coupling strength $b = 3.6$ μs$^{-1}$, correlation time $\tau_c = 25$ μs.[15] Figure 8(a) shows the ensemble ODMR spectrum when the microwave magnetic field is perpendicular to the $\alpha$ axis and the static magnetic field is parallel to the $\alpha$ axis. As the microwave power increases, the broadening becomes larger, which obscures the information of hyperfine coupling. The 3 hyperfine peaks overlap into 1 peak, and the ensemble ODMR spectrum finally presents 2 pairs of resonance peaks.[22] Figure 8(b) shows the $\pi$-pulse width from the Rabi oscillation is 74 ns when the microwave amplitude $B_x = 330$ μT and the microwave frequency $\omega_x = 2813$ MHz.

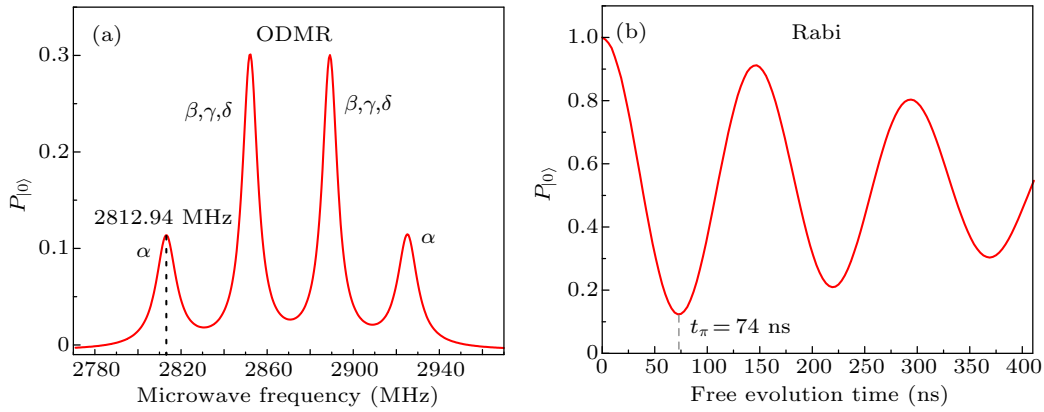



**Fig. 8.** (a) The ensemble ODMR spectrum output by the simulation system, with the abscissa being the microwave frequency and the ordinate being the contrast; (b) The Rabi oscillation curve with the abscissa being the free decay time and the ordinate being the population probability of the $|0\rangle$ state.

### 3.3.1. Axial inhomogeneous distribution

Ideally, the microwave axial direction is perpendicular to the $\alpha$-axis of the ensemble NV centers. In reality, the microwave axial direction has an inhomogeneous distribution in space. We assumed that the axial distribution range is $\theta$, and the number of NV centers is equal per unit angle. In Fig. 6(b), the angle from the purple solid line to the purple dashed line indicates that the axial distribution range of microwaves is 30°. In the model, a group of 12 single NV center modules (to achieve hyperfine coupling effects and spatial orientations of different NV axes) is used to simulate a single microwave deviation angle. Then, the light intensity weighting coefficients module is employed to set $N$ model groups to simulate the axial inhomogeneous distribution of the microwave. Considering both computational power and statistical representativeness, we conducted simulation studies with $N = 4$. For example, when $\theta = 30°$, the axial deviation angles are 0°, 10°, 20°, and 30°. We discussed the cases at $\theta = 0°$, 30°, 60°, and 90°, respectively. Table 2 recorded the output characteristics of the system at different $\theta$.

**Table 2.** Simulation results of inhomogeneity distribution of microwave axial.

| $\theta$ (°) | $\Delta\upsilon$ (MHz) | $C_{\mathrm{ODMR}}$ | $T_2^*$ (ns) | $C_{\mathrm{Ramsey}}$ | $\alpha_{\mathrm{Ramsey}}$ | $T_2$ (ns) | $C_{\mathrm{Hahn}}$ | $\alpha_{\mathrm{Hahn}}$ |
|---|---|---|---|---|---|---|---|---|
| 0 | 11.7 | 0.122 | 427 | 0.78 | 1 | 3370 | 0.29 | 1 |
| 30 | 11.3 | 0.122 | 353 | 0.59 | 1 | 3784 | 0.27 | 1.2 |
| 60 | 10.1 | 0.118 | 263 | 0.33 | 1 | 2883 | 0.19 | 1.2 |
| 90 | 10.3 | 0.089 | 254 | 0.20 | 1 | 2765 | 0.09 | 3 |

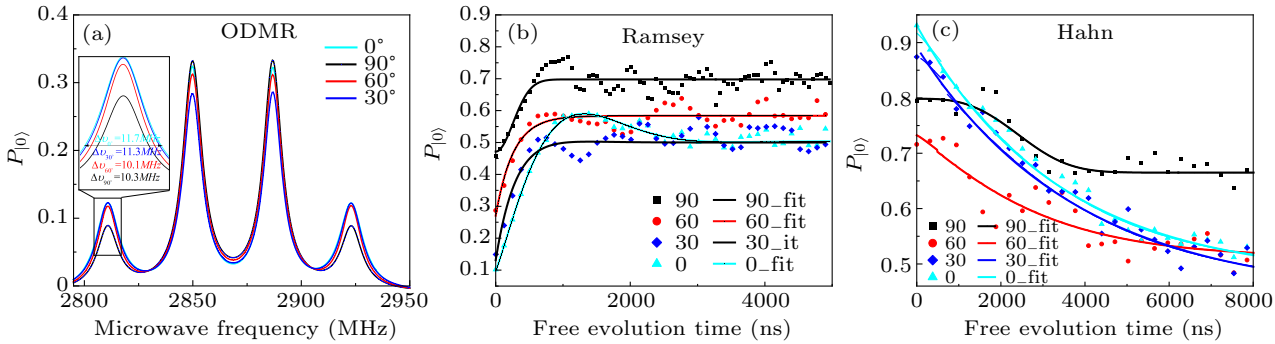



**Fig. 9.** Simulation results of microwave axial inhomogeneity distribution, where the scatter points are simulation data and the solid lines are fitting curves. (a) Ensemble ODMR spectrum, the small diagram at the top left is an enlarged view of a resonance peak; (b) Comparison of ensemble Ramsey curves when the maximum microwave axial deviation angles are 0°, 30°, 60°, and 90°; (c) Comparison of ensemble Hahn echo curves when the maximum microwave axial deviation angles are 0°, 30°, 60°, and 90°.

In a microwave magnetic field, only the component perpendicular to the NV axis can drive spin transitions. The spatial inhomogeneity of the microwave axial direction destroys the consistency of the effective coupling between microwaves and spins, reducing the effective coupling efficiency between microwaves and NV spins. We obtained broadening and contrast by fitting the simulated ODMR curves with a Lorentz function. Figure 9(a) shows that when the maximum deviation angle of axial inhomogeneity is 90°, the resonance peak broadening decreases by 1.4 MHz compared with no deviation, the contrast decreases by 27%, and the sensitivity decreases by 1.2 times according to formula (2). At the same time, inho-

mogeneity will destroy the phase consistency of Ramsey interference, leading to enhanced dephasing effect and reduced contrast. Figure 9(b) shows that when the maximum deviation angle is 90°, the dephasing time decreases from 427 ns to 254 ns, the Ramsey contrast decreases by 74.4%, and the sensitivity decreases by 5.1 times according to formula (2). The core mechanism of the Hahn echo lies in "$\pi$-pulse phase refocusing". However, the axial inhomogeneity of the microwave field disrupts this process. The phases of some NV spins cannot be fully flipped by the $\pi$-pulse, preventing their subsequent phase refocusing. Ultimately, this leads to a decrease in the peak value of the overall echo signal and a reduction in contrast. Figure 9(c) shows that when the maximum deviation angle of the microwave axial direction is 90°, the transverse relaxation time decreases from 3370 ns to 2765 ns, the contrast of the Hahn echo signal decreases by 69%, and the sensitivity decreases by 3.6 times according to formula (2).

### 3.3.2. Amplitude inhomogeneous distribution

The microwave amplitude is inhomogeneously distributed in space, as shown in Fig. 10(a). The yellow block is a diamond containing NV centers, with a size of 5 mm×5 mm×0.5 mm. A microwave magnetic field is applied along the $x$-axis, and a single-loop antenna (SLA) is used to generate the microwave magnetic field.[23] Single NV centers are uniformly distributed within the ensemble NV centers bulk. It is assumed that the microwave amplitude on a small circular ring with a radius of $r$ is equal, and there is a small circular ring area $\mathrm{d}s = \pi(r+\mathrm{d}r)^2 - \pi r^2 \approx 2\pi r\mathrm{d}r$. Then, the number of NV centers on the small circular ring satisfies $N_r \propto \mathrm{d}s \propto r$, based on which the parameters of the light intensity weighting coefficients module can be set in the simulation model. Figure 10(b) The central position and the corresponding microwave amplitude are $(0\ \mathrm{mm}, 330\ \mu\mathrm{T})$. The microwave magnetic field has a linear gradient distribution in space, where $k$ is the slope of the linear distribution gradient.[23,24]

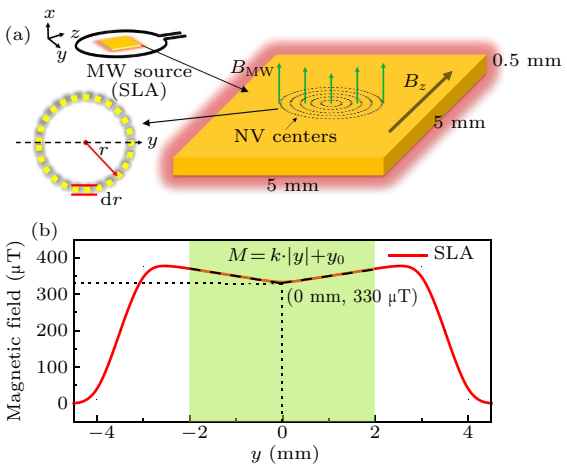



**Fig. 10.** Schematic diagram of the inhomogeneous distribution of microwave amplitude in the diamond ensemble NV centers. (a) Schematic diagram of the microwave magnetic field application device, where the black ring is the microwave antenna, the yellow block is the diamond NV center sample, and the bottom left is a small ring with radius $r$ on the $ZY$ plane; (b) Spatial magnetic field distribution curve of the single-loop antenna (SLA), where the microwave amplitude changes linearly within the range of $y \in [-2\ \mathrm{mm}, 2\ \mathrm{mm}]$.

By setting the microwave amplitude and light intensity weighting coefficients in the simulation model according to different radii, the spatial inhomogeneity of the microwave amplitude can be well simulated. Similarly, considering both computational power and statistical representativeness, we uniformly selected 4 groups of radii for simulation. The radii are 0.5 mm, 1 mm, 1.5 mm, and 2 mm, respectively, and the light intensity weighting coefficients ratios are 0.5:1:1.5:2. We discussed the cases of $k = 0$, 10, 20, 30, 40, and 50 μT/mm, respectively. Table 3 records the output characteristics of the system at different $k$.

**Table 3.** Simulation results of inhomogeneity distribution of microwave amplitude.

| $k$ (μT/mm) | Δυ (MHz) | $C_{\mathrm{ODMR}}$ | $T_2^*$ (ns) | $C_{\mathrm{Ramsey}}$ | $\alpha_{\mathrm{Ramsey}}$ | $T_2$ (ns) | $C_{\mathrm{Hahn}}$ | $\alpha_{\mathrm{Hahn}}$ |
|---|---|---|---|---|---|---|---|---|
| 0 | 11.7 | 0.122 | 427 | 0.78 | 1 | 3370 | 0.29 | 1 |
| 10 | 12.0 | 0.122 | 360 | 0.67 | 1 | 3236 | 0.27 | 1.1 |
| 20 | 12.4 | 0.123 | 323 | 0.45 | 1 | 3916 | 0.26 | 1.4 |
| 30 | 12.7 | 0.124 | 186 | 0.38 | 1 | 4292 | 0.19 | 2.4 |
| 40 | 13.1 | 0.125 | 122 | 0.35 | 1 | 4255 | 0.17 | 2.5 |
| 50 | 13.4 | 0.127 | 103 | 0.31 | 1 | 4389 | 0.14 | 3 |

As the amplitude gradient increases, the frequency consistency of the ensemble NV centers spin transition is broken, resulting in the expansion of the spin resonance frequency distribution range, which is manifested as the inhomogeneity-induced broadening of ODMR. In Fig. 11(a), when $k =$ 50 μT/mm, the linewidth increases by 1.7 MHz compared to the uniform distribution, and the sensitivity decreases by a factor of 1.1. The inhomogeneity of microwave amplitude leads to differences in the spin transition frequencies of different NV centers. After the free spin precession between the two $\pi/2$ pulses, phase dispersion occurs, which manifests as an enhancement of the system's dephasing effect. In Fig. 11(b), when $k = 50$ μT/mm, the dephasing time decreases from 427 ns to 103 ns, the Ramsey contrast decreases by

60.3%, and the sensitivity decreases by a factor of 5.1. Microwave inhomogeneity will cause the pulses to be unable to fully compensate for the phase dispersion caused by the inhomogeneity of the static magnetic field. Pulse sequences such as Hahn echo fail to refocus, resulting in a decrease in echo signal intensity and degradation of coherence. In Fig. 11(c), when $k = 50$ μT/mm, the Hahn echo signal contrast decreases by 51.7%, and the sensitivity decreases by a factor of 1.8. In addition, spatial inhomogeneity will lead to complex decoherence dynamics in the system, which cannot be completely described by a single decay time constant. The stretched exponent $\alpha$ of the ensemble decay ranges from 0.5 to 3,[10] and the higher the spatial inhomogeneity of the microwave magnetic field, the larger fitted $\alpha$.

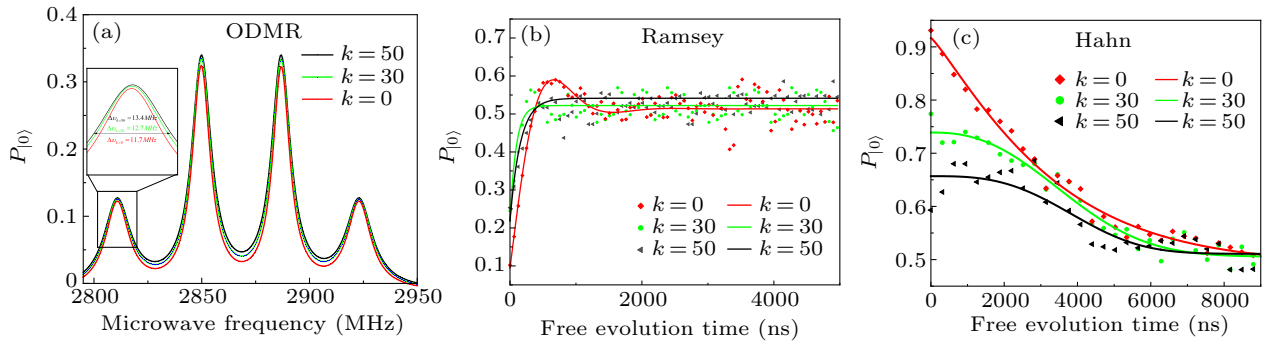



**Fig. 11.** Simulation results of microwave amplitude inhomogeneity distribution, where the scatter points are simulation data and the solid lines are fitting curves. (a) Ensemble ODMR spectrum; the small figure in the upper left corner is an enlarged view of a resonance peak. (b) Comparisons of ensemble Ramsey curves when the microwave amplitude gradients are 0, 30, and 50 μT/mm. (c) Comparisons of ensemble Hahn echo curves when the microwave amplitude gradients are 0, 30, and 50 μT/mm.

## 4. Conclusion

In this work, we designed a multi-module simulation program consisting of a single NV center simulation module and an ensemble control module. By constructing a cage-based diamond NV center experimental system, as well as the verification via ODMR, Ramsey, and Hahn echo experiments, the output curves by the simulation are highly consistent with the experimental data. The model also realizes the ensemble 8-peak ODMR spectrum and the hyperfine coupling effect.

Based on this model, we studied the influence of the inhomogeneous spatial axial and amplitude distributions of the microwave magnetic field on the performance of the ensemble NV centers, respectively. When the axial inhomogeneity of the microwave magnetic field is the largest, the ODMR spectrum contrast decreases by 27%, and the sensitivity decreases by 1.2 times. The dephasing time decreases from 427 ns to 254 ns, the Ramsey contrast decreases by 74.4%, and the sensitivity decreases by 3.9 times. The Hahn echo signal contrast decreases by 69%, and the sensitivity decreases by 3.6 times. When the microwave magnetic field amplitude gradient is $k = 50$ μT/mm, the ODMR spectrum broadening is 1.7 MHz larger than that in the uniform distribution, and the sensitivity decreases by 1.1 times. The dephasing time decreases from 427 ns to 103 ns, the Ramsey contrast decreases by 60.3%, and the sensitivity decreases by 2.52 times. The Hahn echo signal contrast decreases by 51.7%, and the sensitivity decreases by 1.8 times. The model provides quantitative support for microwave parameter optimization, along with a basis for pulse sequence optimization and microwave field uniformity improvement. The modular design facilitates the subsequent inclusion of multi-physics coupling effects, further enhancing the predictive ability of the model. In the future, this model could be combined with artificial intelligence (AI) to develop new pulse sequences and achieve intelligent parameter regulation.

## Appendix A: Theory

When conducting theoretical analysis of NV center quantum sensing, the Hamiltonian energy operator is usually used to analyze, study, and perform theoretical calculations of the quantum spin state. The intrinsic Hamiltonian of the NV center is[25,26]

$$H = \frac{\omega_{\mathrm{D}}}{\hbar} S_z^2 + \gamma_{\mathrm{e}} B \cdot S, \tag{A1}$$

where $\omega_{\mathrm{D}} = 2\pi \times 2.87$ GHz is the zero-field splitting, $\gamma_{\mathrm{e}} = 28.03$ GHz/T is the electron spin gyromagnetic ratio, $\hbar$ is the reduced Planck constant, $\hbar = h/2\pi$, $h$ is the Planck constant, $\boldsymbol{S}$ is the spin operator, $S_x$, $S_y$, $S_z$ are the projection components of $\boldsymbol{S}$ on each coordinate axis, and $\boldsymbol{B}$ is the external magnetic induction field. For a system with spin quantum number $\boldsymbol{S} = 1$, $S_x$, $S_y$, $S_z$ can be expressed as

$$S_x = \frac{\hbar}{\sqrt{2}} \begin{pmatrix} 0 & 1 & 0 \\ 1 & 0 & 1 \\ 0 & 1 & 0 \end{pmatrix}, \quad S_y = \frac{\hbar}{\sqrt{2}} \begin{pmatrix} 0 & -\mathrm{i} & 0 \\ \mathrm{i} & 0 & -\mathrm{i} \\ 0 & \mathrm{i} & 0 \end{pmatrix},$$
$$S_z = \hbar \begin{pmatrix} 1 & 0 & 0 \\ 0 & 0 & 0 \\ 0 & 0 & -1 \end{pmatrix}, \tag{A2}$$

Substituting Eq. (A2) into Eq. (A1) gives

$$H=\hbar\begin{pmatrix}\omega_{\mathrm{D}}+\gamma_{\mathrm{e}}B_z & \frac{\gamma_{\mathrm{e}}}{\sqrt{2}}(B_x-\mathrm{i}B_y) & 0\\ \frac{\gamma_{\mathrm{e}}}{\sqrt{2}}(B_x+\mathrm{i}B_y) & 0 & \frac{\gamma_{\mathrm{e}}}{\sqrt{2}}(B_x-\mathrm{i}B_y)\\ 0 & \frac{\gamma_{\mathrm{e}}}{\sqrt{2}}(B_x+\mathrm{i}B_y) & \omega_{\mathrm{D}}-\gamma_{\mathrm{e}}B_z\end{pmatrix}, \tag{A3}$$

where $B_z$ is the static magnetic field, and $B_x$, $B_y$ are microwave fields applied in different vertical directions. According to the standard Liouville equation of quantum statistical mechanics[27]

$$\frac{\mathrm{d}}{\mathrm{d}t}\tilde{\rho}=\frac{1}{\mathrm{i}\hbar}\left[\tilde{H},\tilde{\rho}\right]-\frac{1}{2}\left\{\hat{\Gamma},\tilde{\rho}\right\}+\Lambda, \tag{A4}$$

where $\mathrm{d}\tilde{\rho}/\mathrm{d}t$ represents the rate of change of the density matrix with time, $\left[\tilde{H},\tilde{\rho}\right]/\mathrm{i}\hbar$ represents the basic evolution process of the quantum system, $(1//2)\left\{\hat{\Gamma},\tilde{\rho}\right\}$ represents the processes of decoherence and dissipation of the quantum state, and $\Lambda$ represents the contribution of additional correction terms or other physical processes.

Introduce the relaxation matrix $\hat{\Gamma}$[27,28]

$$\hat{\Gamma}=\begin{pmatrix}\gamma_1+\Gamma_{\mathrm{p}} & 0 & 0\\ 0 & \gamma_1 & 0\\ 0 & 0 & \gamma_1+\Gamma_{\mathrm{p}}\end{pmatrix}, \tag{A5}$$

where $\gamma_1$ represents the longitudinal relaxation rate, and $\Gamma_{\mathrm{p}}$ represents the transfer rate of non-polarized energy levels to polarized energy levels caused by optical pumping. Substituting the term $(1/2)\left\{\hat{\Gamma},\tilde{\rho}\right\}$ into the Liouville equation (A4) gives

$$\begin{pmatrix}(\gamma_1+\Gamma_{\mathrm{p}})\rho_{11} & (\gamma_1+\Gamma_{\mathrm{p}}/2)\rho_{10} & (\gamma_1+\Gamma_{\mathrm{p}})\rho_{1-1}\\ (\gamma_1+\Gamma_{\mathrm{p}}/2)\rho_{01} & \gamma_1\rho_{00} & (\gamma_1+\Gamma_{\mathrm{p}}/2)\rho_{0-1}\\ (\gamma_1+\Gamma_{\mathrm{p}})\rho_{-11} & (\gamma_1+\Gamma_{\mathrm{p}}/2)\rho_{-10} & (\gamma_1+\Gamma_{\mathrm{p}})\rho_{-1-1}\end{pmatrix}, \tag{A6}$$

where $\rho_{ii}$ is the probability that the quantum system is in the quantum state $|i\rangle$ at a certain moment, and $\rho_{ij}$ characterizes the quantum coherence between different pure states in the quantum system.

Considering that there are other factors affecting the transverse relaxation, after expressing the transverse relaxation with $\gamma_2$ and $\gamma_3$, it is

$$\begin{pmatrix}(\gamma_1+\Gamma_{\mathrm{p}})\rho_{11} & \gamma_2\rho_{10} & \gamma_3\rho_{1-1}\\ \gamma_2\rho_{01} & \gamma_1\rho_{00} & \gamma_2\rho_{0-1}\\ \gamma_3\rho_{-11} & \gamma_2\rho_{-10} & (\gamma_1+\Gamma_{\mathrm{p}})\rho_{-1-1}\end{pmatrix}. \tag{A7}$$

Introduce the repopulation term $\Lambda$[27]

$$\Lambda=\begin{pmatrix}\gamma_1/3 & 0 & 0\\ 0 & \gamma_1/3+\Gamma_{\mathrm{p}}\rho_{11}+\Gamma_{\mathrm{p}}\rho_{-1-1} & 0\\ 0 & 0 & \gamma_1/3\end{pmatrix}, \tag{A8}$$

Substituting Eqs. (A3), (A7), and (A8) into the Liouville equation (A4), and making the following substitutions according to the properties of the density matrix,[25] we have

$$\begin{aligned}&\rho_{11}\to\rho_1,\quad \rho_{00}\to\rho_2,\quad \rho_{-1-1}\to\rho_3,\\ &\rho_{01}\to\rho_4+\mathrm{i}\rho_5,\quad \rho_{10}\to\rho_4-\mathrm{i}\rho_5,\\ &\rho_{0-1}\to\rho_6+\mathrm{i}\rho_7,\quad \rho_{-10}\to\rho_6-\mathrm{i}\rho_7,\\ &\rho_{1-1}\to\rho_8+\mathrm{i}\rho_9,\quad \rho_{-11}\to\rho_8-\mathrm{i}\rho_9.\end{aligned} \tag{A9}$$

Finally, the dynamic equations for the evolution of the density matrix of the three-level model with all real terms can be obtained

$$\begin{aligned}\dot{\rho}_1&=\sqrt{2}\gamma_{\mathrm{e}}(B_x\rho_5-B_y\rho_4)-(\gamma_1+\Gamma_{\mathrm{p}})\rho_1+\frac{\gamma_1}{3},\\ \dot{\rho}_2&=\sqrt{2}\gamma_{\mathrm{e}}[B_y(\rho_4-\rho_6)-B_x(\rho_5+\rho_7)]\\ &\quad-\gamma_1\rho_2+\frac{\gamma_1}{3}+\Gamma_{\mathrm{p}}(\rho_1+\rho_3),\\ \dot{\rho}_3&=\sqrt{2}\gamma_{\mathrm{e}}(B_x\rho_7+B_y\rho_6)-(\gamma_1+\Gamma_{\mathrm{p}})\rho_3+\frac{\gamma_1}{3},\\ \dot{\rho}_4&=-\frac{\gamma_{\mathrm{e}}}{\sqrt{2}}[B_x\rho_9+B_y(\rho_2-\rho_1+\rho_8)]-\gamma_2\rho_4-(\omega_{\mathrm{D}}+\gamma_{\mathrm{e}}B_z)\rho_5,\\ \dot{\rho}_5&=\frac{\gamma_{\mathrm{e}}}{\sqrt{2}}[B_y\rho_9-B_x(\rho_1-\rho_2+\rho_8)]-\gamma_2\rho_5+(\omega_{\mathrm{D}}+\gamma_{\mathrm{e}}B_z)\rho_4,\\ \dot{\rho}_6&=\frac{\gamma_{\mathrm{e}}}{\sqrt{2}}[B_x\rho_9+B_y(\rho_2-\rho_3+\rho_8)]-\gamma_2\rho_6-(\omega_{\mathrm{D}}-\gamma_{\mathrm{e}}B_z)\rho_7,\\ \dot{\rho}_7&=\frac{\gamma_{\mathrm{e}}}{\sqrt{2}}[B_y\rho_9+B_x(\rho_2-\rho_3-\rho_8)]-\gamma_2\rho_7+(\omega_{\mathrm{D}}-\gamma_{\mathrm{e}}B_z)\rho_6,\\ \dot{\rho}_8&=\frac{\gamma_{\mathrm{e}}}{\sqrt{2}}[B_x(\rho_5+\rho_7)+B_y(\rho_4-\rho_6)]-\gamma_3\rho_8+2\gamma_{\mathrm{e}}B_z\rho_9,\\ \dot{\rho}_9&=\frac{\gamma_{\mathrm{e}}}{\sqrt{2}}[B_x(\rho_4-\rho_6)-B_y(\rho_5+\rho_7)]-\gamma_3\rho_9-2\gamma_{\mathrm{e}}B_z\rho_8.\end{aligned} \tag{A10}$$

According to the characteristics of the density matrix, its diagonal elements $\rho_{11}$, $\rho_{00}$, $\rho_{-1-1}$ are the probabilities, *i.e.*, the populations, of the quantum system being in the $|+1\rangle$, $|0\rangle$, $|-1\rangle$ states at a certain moment, and the trace of the matrix always satisfies $\rho_{11}+\rho_{00}+\rho_{-1-1}=1$.

Since the probability of radiative transition of electrons in the $|0\rangle$ state after pumping is relatively high, while the probability of electrons in the $|\pm1\rangle$ states returning to the ground state through intersystem crossing (ISC) after pumping is relatively high, it can be considered that the radiative fluorescence intensity is proportional to the population numbers $\rho_{00}$, $\rho_{11}$, $\rho_{-1-1}$ of the three energy levels, but the proportionality coefficients are different, which are $\alpha$, $\beta$, $\beta$ respectively, and $\alpha>\beta$. Therefore, the fluorescence intensity measured in the experiment can be expressed as[29]

$$I=\alpha\rho_{00}+\beta(\rho_{11}+\rho_{-1-1})=(\alpha-\beta)\rho_{00}+\beta. \tag{A11}$$

For the given set of equations for the density matrix evolution dynamics, to solve this ordinary differential equation, we consider using the RK4 algorithm[30]

$$y'=f(t,y),$$

$$
\begin{aligned}
&y_{n+1} = y_n + \frac{h}{6}(k_1 + 2k_2 + 2k_3 + k_4),\\
&k_1 = f(t_n, y_n),\\
&k_2 = f(t_n + h/2, y_n + k_1 h/2),\\
&k_3 = f(t_n + h/2, y_n + k_2 h/2),\\
&k_4 = f(t_n + h, y_n + k_3 h).
\end{aligned} \tag{A12}
$$

For Eq. (A12) multiple coupled equations, there are

$$
\begin{aligned}
&\dot{\rho}_i = f_i\left(t, \{\rho_j\}\right),\\
&\rho_{i,n+1} = \rho_{i,n} + \frac{h}{6}(k_{i,1} + 2k_{i,2} + 2k_{i,3} + k_{i,4}),\\
&k_{i,1} = f_i\left(t_n, \{\rho_{j,n}\}\right),\\
&k_{i,2} = f_i\left(t_n + h/2, \{\rho_{j,n} + k_{j,1} h/2\}\right),\\
&k_{i,3} = f_i\left(t_n + h/2, \{\rho_{j,n} + k_{j,2} h/2\}\right),\\
&k_{i,4} = f_i\left(t_n + h, \{\rho_{j,n} + k_{j,3} h\}\right).
\end{aligned} \tag{A13}
$$

When solving the density matrix dynamics equation, the RK4 algorithm has high precision, high stability, and simplicity of implementation. It has significant advantages in balancing accuracy and computational cost and handling the evolution of complex quantum systems.

## Acknowledgements

Project supported by the Autonomous Scientific Research of the College of Frontier Interdisciplinary Sciences, the National University of Defense Technology (Grant No. ZZKY2023-01) and the Research on Key Technologies of Diamond NV Center Clocks.

## References

[1] Degen C L, Reinhard F and Cappellaro P 2017 *Rev. Mod. Phys.* **89** 035002
[2] Doherty M W, Manson N B, Delaney P, Jelezko F, Wrachtrup J and Hollenberg L C L 2013 *Phys. Rep.* **528** 1
[3] Du J, Shi F, Kong X, Jelezko F and Wrachtrup J 2024 *Rev. Mod. Phys.* **96** 025001
[4] Jelezko F and Wrachtrup J 2006 *Physica Status Solidi (a)* **203** 3207
[5] Hanson R, Dobrovitski V V, Feiguin A E, Gywat O and Awschalom D D 2008 *Science* **320** 352
[6] Doherty M W, Manson N B, Delaney P and Hollenberg L C L 2011 *New Journal of Physics* **13** 025019
[7] Lovchinsky I, Sushkov A O, Urbach E, *et al*. 2016 *Science* **351** 836
[8] Lovchinsky I, Sanchez-Yamagishi J D, Urbach E K, *et al*. 2017 *Science* **355** 503
[9] Pham L M 2013 *Magnetic field sensing with nitrogen-vacancy color centers in diamond*, Ph.D. Dissertation (Cambridge: Harvard University)
[10] Barry J F, Schloss J M, Bauch E, Turner M J, Hart C A, Pham L M and Walsworth R L 2020 *Rev. Mod. Phys.* **92** 015004
[11] Popa I, Gaebel T, Domhan M, Wittmann C, Jelezko F and Wrachtrup J 2004 *Phys. Rev. B* **70** 201203
[12] Dreau A, Lesik M, Rondin L, Spinicelli P and Arcizet O 2011 *Phys. Rev. B* **84** 195204
[13] Cao Q Y 2024 *Concatenated Continuous Dynamical Decoupling Based on Nitrogen-Vacancy Color Centers in Diamond*, Ph. D. Dissertation (Wuhan: Huazhong University of Science and Technology) (in Chinese)
[14] Stern H L, M. Gilardoni C, Gu Q, *et al*. 2024 *Nat. Mater.* **23** 1379
[15] De Lange G, Wang Z H, Ristè D, Dobrovitski V V and Hanson R 2010 *Science* **330** 60
[16] Ghassemizadeh R, Körner W, Urban D F and Elsässer C 2024 *Phys. Rev. B* **110** 205148
[17] Abeywardana C, Stepanov V, Cho F H and Takahashi S 2016 *J. Appl. Phys.* **120** 123907
[18] Yang Y, Wu Q, Wang Y, Chen W, Yu Z, Yang X, Fan J W and Chen B 2023 *Opt. Contin.* **2** 1426
[19] Bayat K, Choy J, Farrokh Baroughi M, Meesala S and Loncar M 2014 *Nano Lett.* **14** 1208
[20] Wang P 2015 *Decoherence Theory in Nitrogen-Vacancy Color Centers and Its Applications*, Ph.D. Dissertation (Hefei: University of Science and Technology of China) (in Chinese)
[21] Simanovskaia M, Jensen K, Jarmola A, Aulenbacher K, Manson N and Budker D 2013 *Phys. Rev. B* **87** 224106
[22] Tahara K, Ozawa H, Iwasaki T, Mizuochi N and Hatano M 2015 *Appl. Phys. Lett.* **107** 193110
[23] Chen Y, Li T, Chai G, Wang D, Lu B, Guo A and Tian J 2022 *Nanomaterials* **12** 3938
[24] Meinel J, Vorobyov V, Yavkin B, Dasari D, Sumiya H, Onoda S, Isoya J and Wrachtrup J 2021 *Nat. Commun.* **12** 2737
[25] Appelt S, Ben-Amar Baranga A, Young A R and Happer W 1999 *Phys. Rev. A* **59** 2078
[26] Jensen K, Acosta V M, Jarmola A and Budker D 2013 *Phys. Rev. B* **87** 014115
[27] Rochester S M 2010 *Modeling nonlinear magneto-optical effects in atomic vapors*, Ph.D. Dissertation (Berkeley: University of California)
[28] Alipieva E A, Taskova E T, Todorov G Ts, Polishchuk V A and Vartanyan T A 2019 *Optics and Spectroscopy* **127** 395
[29] Tetienne J P, Rondin L, Spinicelli P, Chipaux M, Debuisschert T, Roch J F and Jacques V 2012 *New J. Phys.* **14** 103033
[30] Milstein G N and Tretyakov M V 2021 *Stochastic Numerics for Mathematical Physics* (Cham: Springer International Publishing), pp. 203–204